Steel and Composite Structures, Vol. 2, No. 3 (2002) 171-194
DOI: http://dx.doi.org/10.12989/scs.2002.2.3.171

Finite element modelling and design of partially encased composite columns

Thierry Chicoine†, Robert Tremblay‡ and Bruno Massicotte‡

Department of Civil, Geological, and Mining Engineering, Ecole Polytechnique, Montreal, H3C 3A7, Canada

(Received September 1, 2001, Accepted May 1, 2002)

Abstract. In this paper, the behaviour of axially loaded partially encased composite columns made with light welded *H* steel shapes is examined using ABAQUS finite element modelling. The results of the numerical simulations are compared to the response observed in previous experimental studies on that column system. The steel shape of the specimens has transverse links attached to the flanges to improve its local buckling capacity and concrete is poured between the flanges only. The test specimens included 14 stub-columns with a square cross section ranging from 300 mm to 600 mm in depth. The transverse link spacing varied from 0.5 to 1 times the depth and the width-to-thickness ratio of the flanges ranged from 23 to 35. The numerical model accounted for nonlinear stress-strain behaviour of materials, residual stresses in the steel shape, initial local imperfections of the flanges, and allowed for large rotations in the solution. A Riks displacement controlled strategy was used to carry out the analysis. Plastic analyses on the composite models reproduced accurately the capacity of the specimens, the failure mode, the axial strain at peak load, the transverse stresses in the web, and the axial stresses in the transverse links. The influence of applying a typical construction loading sequence could also be reproduced numerically. A design equation is proposed to determine the axial capacity of this type of column.

Key words: composite column; built-up steel shape; local buckling; finite element models; materials behaviour; section capacity; design equations.

1. Introduction

A new type of partially encased composite (PEC) column consisting of thin-walled, *I*-shaped steel section with concrete poured between the flanges of the steel section has recently been developed and patented by the Canam Manac Group (Figs. 1 and 2). The steel section uses very slender plates exceeding the width-to-thickness ratio limits for non-compact sections. Transverse links between the flanges are spaced at regular intervals, *s*, to enhance the resistance of the flanges to local buckling. The proposed PEC column is intended to essentially carry axial loads in multi-storey buildings, the lateral loads being resisted by other structural systems such as shear walls.

The advantages of this system over traditional composite column design have been presented by Vincent (2000) and several series of axial loading tests have been performed on large-scale columns (Tremblay *et al*. 1998, Chicoine *et al*. 2000a, 2002a). Failure of test columns occurred by crushing of

†Former Graduate Research Assistant
‡Professor

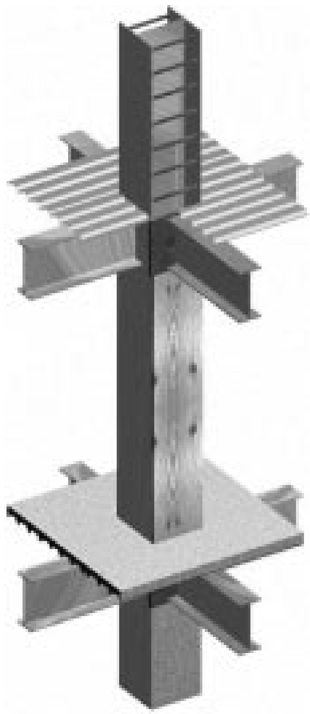

Fig. 1 Partially encased composite (PEC) column under construction

the concrete accompanied with yielding and local buckling of the steel shapes. In specimens with larger width-to-thickness ratio, *b/t*, and link spacing-to-depth ratio, *s/d*, local buckling of the flanges occurred before the peak load was reached. A series of tests (Chicoine *et al*. 2000b, 2002b) was also performed to investigate the influence of construction loading sequence and examine the long-term behaviour of these columns. Design equations accounting for local flange buckling have been proposed by Tremblay *et al*. (1998, 2000), and Chicoine *et al*. (2002a).

Finite element models of partially encased composite columns were initiated by Maranda (1999) using the computer program MEF (Bouzaiene and Massicotte 1997). By taking advantage of the double symmetry of the column, only a quarter of the cross section was modelled, including the local imperfections of the steel flange and the residual stresses. The model by Maranda reproduced adequately the experimental axial capacity of test specimens, with an average ratio of experimental to numerical peak loads of 0.95, and a standard deviation of 0.03. In most of the analyses, however, the post-peak response could not be obtained. Broderick and Elnashai (1994) studied the seismic behaviour of partially encased composite columns having a compact steel section and transverse links when subjected to inelastic earthquake loading. The reference test specimens had various axial load levels and were tested under dynamic and pseudo-dynamic protocols. The authors proposed a numerical model using the computer program ADAPTIC. This program featured three types of concrete confinement: unconfined concrete between the exposed face and the transverse links, fully-confined concrete near the web of the steel shape, and partial confinement for the concrete located between these two regions. The authors did not introduce the residual stresses nor the local imperfections in the steel shape. Good agreement with experimental results was obtained for the ultimate moment as well as the

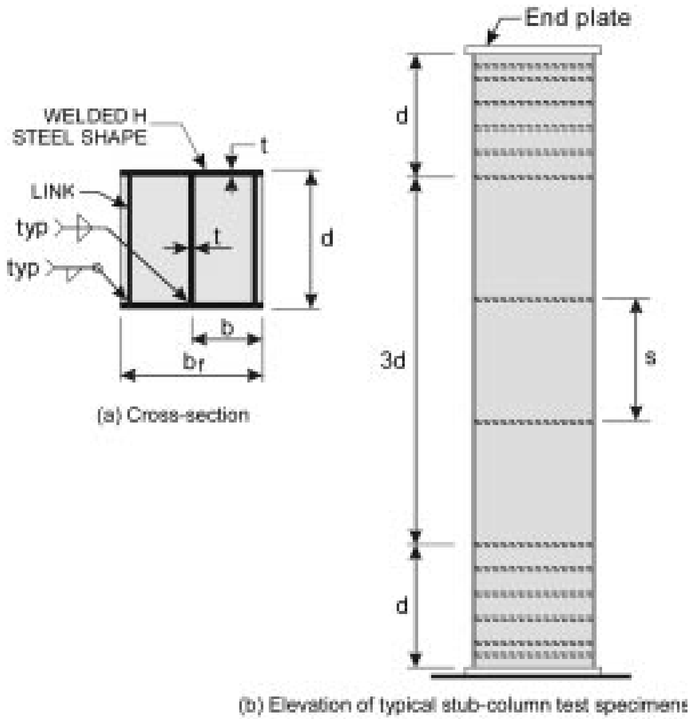

Fig. 2 Geometry of partially encased columns

displacement and rotation ductility, and the seismic efficiency for this type of composite system could be demonstrated. The finite element program ABAQUS was used by Sigiura *et al*. (2000) in modelling a composite sandwich beam that had been tested in flexure. The interface between the concrete and the reinforcing material on the tension side of the cross-section was modelled using a set of non-linear springs in the three principal directions of the coordinate system. The concrete part was modelled using 20-node quadratic brick elements with reduced integration (C3D20R).

2. Objectives and scope of the research

The objectives and scope of this study were to examine several aspects of the behaviour of PEC columns using finite element (FE) techniques to recommend design equations for the axial capacity of the columns. A model was first developed with the computer program ABAQUS (HKS, 2000) to reproduce the experimental behaviour of 14 full-scale stub-columns: strain at peak load, transverse stresses in the web of the steel shape, tensile force in transverse links, local buckling behaviour of the steel plates, loading sequence and long term effects. The model allowed for large displacements in the solution and included the following features: non-linear stress-strain behaviour of materials, residual stresses in the steel shape, initial local imperfections of the flanges, and contact elements between the concrete and the steel web. The model was then used to examine the influence of residual stresses, initial local imperfections, and sequence of loading. The results permitted to develop a design equation to accurately predict the axial load capacity of the PEC columns.

3. Reference test database

Tests on 14 partially encased composite column specimens were selected from the experimental programs performed by Tremblay *et al*. (1998) and Chicoine *et al*. (2002a, 2002b) for the purpose of verifying the FE models developed in this study. Table 1 gives the characteristics of these columns (see also Fig. 2), including the yield stress of the steel, F_y, as well as the ultimate strength, f'_c, the elastic modulus, E_c, and the strain at peak load, ε'_c, of the concrete, as measured from tests on cylinders. The selection covers the full range of the main geometric parameters of the columns, i.e. the column depth, *d*, the width-to-thickness ratio of the flanges, *b/t*, and the relative spacing of the transverse links, *s/d*. Test series 1 and 2 were short-term axial tests on partially encased composite columns with a cross section ranging from 300 mm×300 mm to 600 mm×600 mm. The sequence of construction and long-term behaviour of the column system was examined on 300 mm×300 mm and 450 mm×450 mm columns in Test Series 3. Specimens C-3 and C-6 in Series 1, which had a link spacing of 3*d*/4, were not modelled but the results from these tests are used later to validate the proposed design equations.

The loading sequence for specimens of Series 3 included a total of three stages, as illustrated in Fig. 3. At Stage 1, an axial load was applied to the steel shape only by tensioning the high strength bolts to induce a nominal compressive stress of 100 MPa before concreting. This stress corresponds to the maximum anticipated effects of typical construction loading carried by the steel shape alone. At Stage 2, 14 days after pouring the concrete, the applied load was increased to reach the anticipated axial load due to the long-term service load: 100% Dead load+50% Live load. This load was maintained for a period of approximately 6 months and produced a total stress of 170 MPa in the steel and 10 MPa in the concrete. At Stage 3, the load on the composite column was increased further up to failure.

Table 1 Properties of test specimens

Test Series	No.	$b_f \times d \times t$ (mm)	Height (mm)	*b/t* ( )	*s* (mm)	Link ϕ (mm)	f'_c (MPa)	E_c (MPa)	ε'_c (me)	F_y (MPa)
1 (Small Specimens)	C-2	450×450×9.70	2 250	23.2	225	12.7	32.7	28 000	2 250	370
	C-3	450×450×9.70	2 250	23.2	338	12.7	32.4	28 000	2 250	370
	C-4	450×450×9.70	2 250	23.2	450	12.7	31.9	28 000	2 250	370
	C-5	450×450×9.70	2 250	23.2	225	22.2	34.3	28 000	2 250	370
	C-6	450×450×6.35	2 250	35.4	338	12.7	32.7	28 000	2 250	374
	C-7	300×300×6.35	1 500	23.6	300	12.7	31.9	31 500	2 250	374
2 (Large Specimens)	C-8	600×600×12.90	3 000	23.3	600	16.0	34.2	27 300	2 000	360
	C-9	600×600×12.90	3 000	23.2	600	16.0	34.2	27 300	2 000	360
	C-10	600×600×12.80	3 000	23.4	300	16.0	34.2	27 300	2 000	360
	C-11	600×600×9.70	3 000	30.9	600	16.0	34.2	27 300	2 000	345
	C-12*	600×600×12.90	3 000	23.3	300	16.0	34.2	27 300	2 000	360
3 (Long-Term Specimens)	P-1	300×300×6.50	1 500	23.6	300	12.7	36.9	29 950	2 470	390
	P-2	300×300×6.50	1 500	23.6	300	12.7	36.9	29 950	2 470	390
	P-3	300×300×6.50	1 500	23.6	300	12.7	36.9	29 950	2 470	390
	P-4	300×300×6.50	1 500	23.6	300	12.7	36.9	29 950	2 470	390
	P-5	450×450×9.60	2 350	23.2	450	12.7	30.0	29 950	2 470	345

Note: *With additional reinforcement: 4-20 M longitudinal rebars, and pairs of *U*-stirrups 15 M@300 mm.

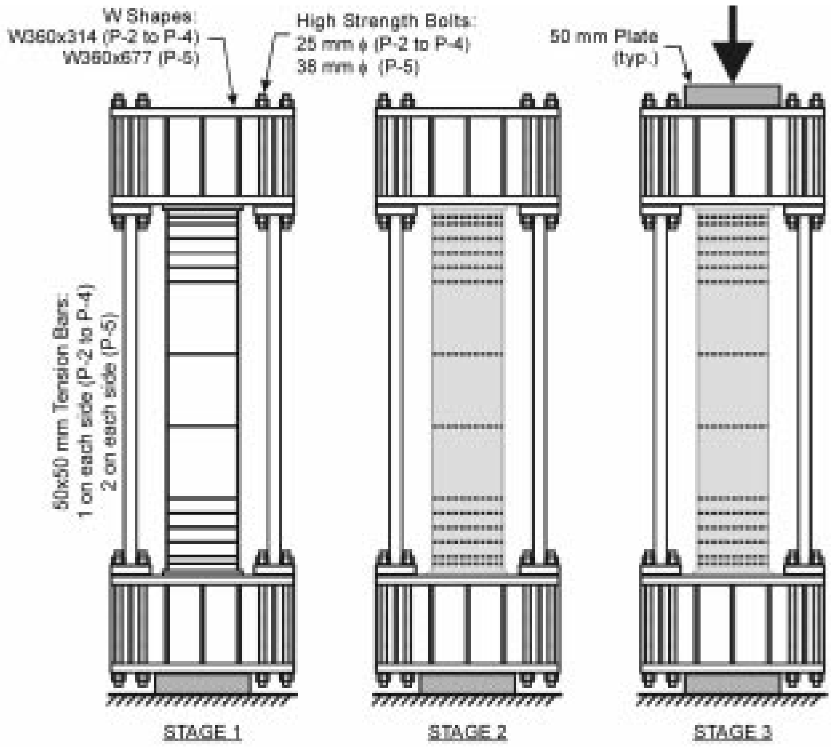

Fig. 3 Loading stages 1 to 3

4. Characteristics of the finite element models

4.1. Geometric properties

By making use of the symmetry of the cross section, the finite element models only included a quarter of the cross section, over a height of one transverse link spacing (Fig. 4a). As described later, the peak load was reached in test columns upon failure on one side of the web only. This failure was symmetrical about the strong axis of the steel shape and a model including one quarter of the section was adequate to reproduce this behaviour. The complete models are presented in Figs. 4b and 4c for link spacing of $s = d/2$ and $s = d$, respectively. Eight-node shell elements (S8R) were used to model both the flange and the web. This element type was preferred over a four-node shell element because it provides a better prediction of the buckling capacity of the steel shape for the same number of elements. In the model with $s = d/2$, the mesh for the flange and the web each had 7 elements over the width and 6 elements over the height (84 elements total). The size of 72 shell elements matched that of the adjacent concrete elements and each had a length-to-width ratio close to the optimal value of one. A convergence study was also performed to optimize the number of elements. Near the connection between the flange and the web in the specimens, narrower plate elements extended both the flange and the web over a width equal to half the plate thickness to connect to the centreline of each plate. Using such narrow elements did not downgrade the quality of the solution since they were away from the buckling zone and were expected to carry axial load only. A mesh of 6×6×6 type C3D20R solid elements (216 elements total)

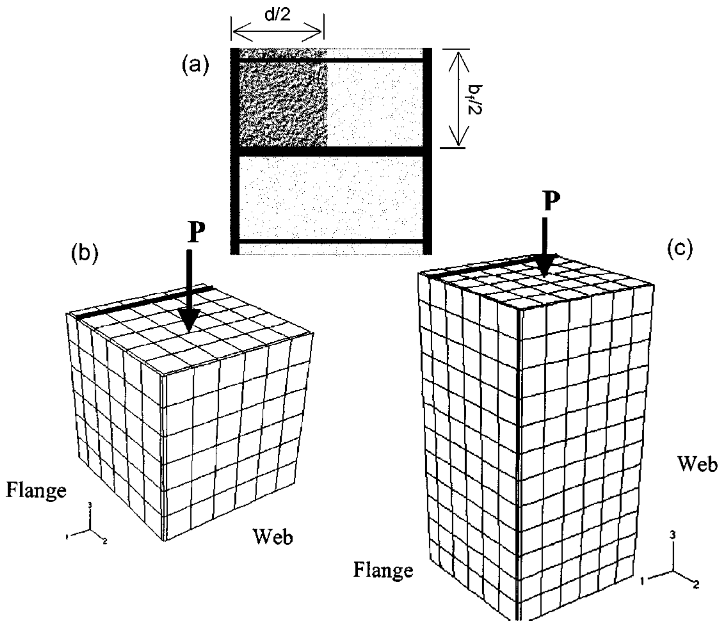

Fig. 4 Finite element models of the column: (a) Quarter cross section; (b) Specimen with s=d/2; and (c) Specimen with s = d.

was used to model the concrete. This 3D solid element type has a total of 20 nodes, with 8 nodes on each face. This permitted a perfect node-by-node match with the S8R shell elements, enabling to capture well the interaction between the steel and the concrete. The transverse links at the top and bottom ends of the models were made up of 7 type B32 beam type elements (14 elements total). This beam element type has three nodes and the length of each of these elements matched the width of the adjacent concrete elements, except between the steel flange and the concrete where the length of the link was equal to half the flange thickness. The same configuration was used for the model with s = d except that the number of elements was doubled in the longitudinal direction, effectively doubling the total number to 168 shell and 432 solid elements.

Two-node spring elements of type Spring 2 were introduced at every nodal point between the steel flange and the opposing concrete face. These elements were given a very high stiffness in compression to prevent inward buckling of the flange due to the presence of the concrete, and a very low tensile stiffness to allow the flange to buckle freely in the outward direction. The displacements of the nodes in the web shell elements and the adjacent concrete face were coupled in directions 1 and 3 by means of stiff Spring 2 elements to simulate perfect contact between the concrete and the steel web. All nodes of the transverse links were coupled to the adjacent concrete nodes in the axial direction of the links, to simulate the perfect bond between the links and the concrete transverse expansion and permit the development of tensile stresses in the links.

On the loaded face, the vertical displacement of all nodes were constrained to be the same as that of the node to which the load was applied. On the bottom face, vertical displacement were prevented at all nodes. Displacements in both transverse directions were free at the top and bottom faces. Usual modelling rules for boundary conditions were applied along the planes of symmetry.

4.2. Material mechanical properties

A bilinear strain-stress behaviour was assumed for steel, with an elastic modulus of 200 GPa, a yield stress, F_y, as given in Table 1, and a strain hardening slope of 800 MPa, based on typical stress-strain curves obtained from tensile tests on steel coupons. The mechanical properties assigned to the concrete elements are presented in Table 2. The analyses were made with an effective concrete strength, f'_{ce}, and an effective elastic modulus, E_{ce}, given by:

$$f'_{ce}=0.92\Psi f'_c \tag{1}$$

$$E_{ce}=\sqrt{0.92\Psi}\,E_c \tag{2}$$

where f'_c and E_c are respectively the concrete strength and elastic modulus measured from cylinders at the day of column testing. The parameter Ψ was proposed by Chicoine *et al*. (2002a), based on experimental data reported by Neville (1966), to account for the size effect on the concrete strength in PEC columns:

$$\psi = 0.85\left(0.96+\frac{22}{b}\right)\begin{cases}\geq 0.85\\ \leq 0.97\end{cases} \tag{3}$$

The parameter b in Eq. (3) is in mm. The reduction factor 0.92 mainly accounts for the lower quality of the concrete used in structural elements when compared to the concrete in test cylinders. Such difference arises from variation in compaction, handling, workmanship, and curing methods (Newman 1987). As discussed later, the value of 0.92 was obtained through an iterative process until an average test-to-predicted ratio of 1.0 was obtained for all test specimens. This value confirms the finding by

Table 2 Properties of numerical model

Test Series	No.	$b'_f \times d' \times t'_f$ (mm)	t'_w (mm)	$L' = s$ (mm)	δ_{0m} Mean (mm)	δ_{0m} S.D. (mm)	f'_{ce} (MPa)	E_{ce} (MPa)
1 (Small Specimens)	C-2	225×220.15×9.7	4.85	225	0.39	0.13	27.1	25 460
	C-4	225×220.15×9.7	4.85	450	1.42	0.23	26.4	25 460
	C-5	225×220.15×9.7	4.85	225	0.39	0.13	28.4	26 190
	C-7	150×146.8×6.4	3.20	300	0.63	0.20	27.6	29 310
2 (Large Specimens)	C-8	300×293.6×12.9	6.45	600	1.43	1.38	27.6	24 540
	C-9	300×293.6×12.9	6.45	600	2.02	0.36	27.6	24 540
	C-10	300×293.6×12.8	6.40	300	0.38	0.15	27.6	24 540
	C-11	300×293.6×9.7	4.85	600	0.71	0.46	27.6	24 540
	C-12*	300×293.6×12.9	6.45	300	0.37	0.15	27.6	24 540
3 (Long-Term Specimens)	P-1	150×146.8×6.5	3.25	300	0.74	0.35	31.8	27 870
	P-2	150×146.8×6.5	3.25	300	0.58	0.27	31.8	27 870
	P-3	150×146.8×6.5	3.25	300	0.35	0.19	31.8	27 870
	P-4	150×146.8×6.5	3.25	300	0.44	0.16	31.8	27 870
	P-5	225×220.2×9.6	4.80	450	0.52	0.13	24.8	22 400

Note: Steel yield stress, F_y, and concrete peak strain, ε'_c, as in specimens

Maranda (1999) that material strength has to be reduced in the numerical model to match more precisely the test results. This reduction factor is also in line with the value of 0.9 proposed by Bloem (1968) and with the provisions included in modern standards for the design of concrete structures. For instance, in CSA-A23.3 Standard (1994a), a factor of 0.9 has been included in the design equation for reinforced concrete columns to account for this difference between cylinder and structure concrete.

The stress-strain relationship of the concrete in uniaxial compression was defined in 100 $\mu\varepsilon$ increments by adjusting the parameters in the formulation proposed by Tsai (1988) to match the measured peak strain (Table 1) and the effective elastic modulus and strength (Table 2). The tensile strength of the concrete was set to 9% of the compressive strength in the model. The Poisson's ratio of steel was taken as 0.3. For concrete, that ratio was set equal to 0.18 in the elastic range (up to 40% f'_{ce}), and thereafter increased linearly up to 0.45 at peak stress. The value of 0.18 was obtained from measurements on cylinders in test Series 1 to 3, while the final value is the maximum value that can be obtained from the program built-in concrete model, based on solid mechanics. Fig. 5 compares the Poisson's ratios obtained from concrete cylinders of Series 3 and the FE concrete model. The figure shows that the Poissonís ratio in the cylinders starts increasing at about 500 $\mu\varepsilon$, and exceeds that of the steel for strains greater than 1,000 $\mu\varepsilon$. Good agreement is obtained between the concrete prediction model and the experimental values up to about 1,000 $\mu\varepsilon$. Near peak strain, the model underestimates the lateral expansion of the cylinders because the concrete of the cylinders no longer is a homogeneous material after extensive cracking has developed.

No cylinders were tested at the day of testing for Specimen P-5. The concrete strength was extrapolated from measurements at an earlier age (Chicoine *et al.* 2002b) and the elastic modulus was taken equal to 4,500 $\sqrt{f'_c}$. Therefore, the mechanical properties of the concrete for this specimen are approximate.

4.3. Initial out-of-straightness and residual stresses in the steel shape

Measured out-of-straightness of the flanges of the specimen steel shape, δ_{0m}, varied from 0.35 mm (P-3) to 2.02 mm (C-9), which corresponds to s/875 and s/297, respectively. On specimens with a link spacing of d/2, the mean imperfection was s/670 (standard deviation, SD, of s/1870), a value smaller than for specimens with a spacing of d: $\delta_{0m} = s/500$ with SD of s/1200. When considering all link spacings, however, similar mean imperfections were found in small and large specimens (s/550 vs. s/530). Due to the fabrication process, the imperfections were typically inwards, resulting in a

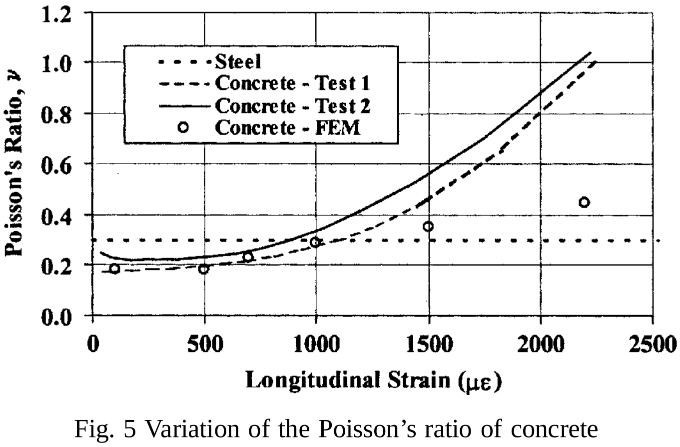

Fig. 5 Variation of the Poisson's ratio of concrete

favourable condition for resistance to local buckling. In the FE models, these initial deformations of the steel flanges were included by applying a deformed shape corresponding to the first buckling mode obtained from eigenvalue analysis performed on models that included only the steel shape. The deformed shape was then scaled to match the value of δ_{0m} measured for each specimen, as given in Table 2. Preliminary analyses indicated that setting the imperfection inwards resulted in a buckling mode of the flange that was different from that observed experimentally. Near failure, lateral expansion of the concrete in the test columns exceeded that in the model (see Fig. 5) and likely forced the flanges to buckle outwards. The imperfections were therefore set outwards in the FE models to reproduce the observed behaviour. This assumption is conservative and is justified later by the analysis results.

Typical residual stresses measured on the specimen steel shapes are shown in Fig. 6. Also given in the figure are the amplitude and distribution of the residual stresses that were adopted in the analytical models. The residual stresses are characterised by high tensile values at the welds connecting the flanges to the web and compressive values away from the welds. The residual stresses were introduced in the numerical models as uniform initial axial stresses in each of the shell element of the flange and web. As shown, the compression residual stresses could be reproduced accurately in the model but

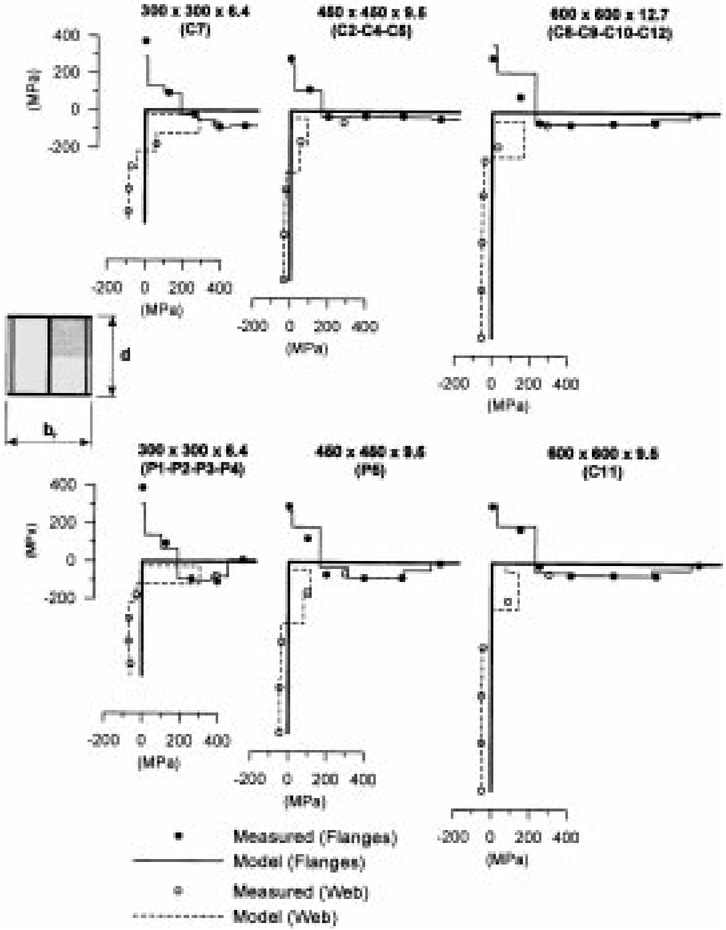

Fig. 6 Residual stresses in the steel shapes

some error was introduced for the tensile stresses because the sharp gradient exhibited by the experimental stresses could not be captured adequately due to the size of the elements. In addition, equilibrium between tension and compression residual stresses in the models was obtained by adjusting only the tensile stresses, as the compression values were considered more reliable. For some columns, this contributed in increasing further the difference between experimental and numerical tensile residual stresses.

4.4. Sequence of loading and analysis strategy

For reproducing the various loading stages in the long-term test series (specimens P-2 to P-5), the model was first entirely defined with the concrete and the steel elements. The concrete elements were then removed and the steel shape was first loaded to match the long-term stresses. The concrete elements were put back in place and the load was increased further on the composite section in Stages 2 and 3. The long-term effects on the concrete were not modelled directly using the program built-in creep models. Instead, the long-term deformations were taken into account by adding the stress increase measured in the steel in loading Stage 2 during testing to the stresses applied at Stage 1 in the model. So doing, the stresses in both materials at the end of Stage 2 corresponded to the stresses obtained experimentally, as shown in Table 3. In loading Stage 3, the load was increased up to failure.

The solution strategy in the analysis was a Riks displacement control scheme, with an initial arc length increment corresponding to 10% of the ultimate load. This method is best suited for nonlinear or unstable problems, such as the inelastic buckling of a plate, and generally permits to determine the post-peak response of a structural model.

5. Plastic analysis of the composite sections

5.1. Prediction of failure modes and ultimate capacity

Typical failure modes for specimens with $s=d$ (Specimen C-8) and $s=d/2$ (Specimen C-12) are given in Fig. 7. Peak load was attained when failure occurred by crushing of the concrete with local buckling of the flanges that developed between two adjacent transverse links on one side of the column. This was immediately followed by a similar failure on the opposite side, within the adjacent link spacing. No concrete spalling was observed before peak load. Table 4 presents the results of the plastic analysis of

Table 3 Stresses in materials according to loading sequence

Spec.	Experimental stresses			FE stresses		
	Stage 1	Stage 2			Stage 2	
	Steel (MPa)	Steel (MPa)	Concrete (MPa)	Steel (MPa)	Steel (MPa)	Concrete (MPa)
P-1	-	-	-	-	-	-
P-2	100	111	-	110	110	-
P-3	101	215	6.8	167	213	6.8
P-4	101	219	6.5	173	218	6.5
P-5	103	223	6.5	164	222	6.5

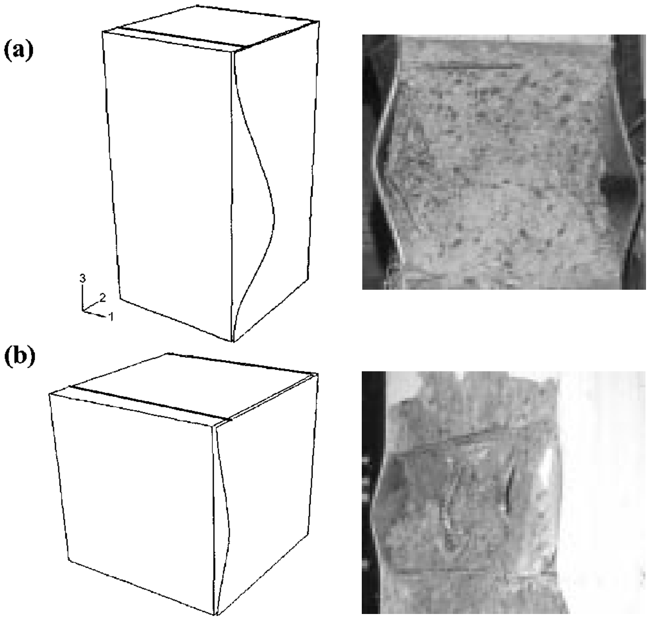

Fig. 7 Predicted and experimental failure modes for specimens with: (a) $s=d$; (b) $s=d/2$

the composite models. In the table, the squash load of the column, neglecting local buckling effects, P_0, corresponds to:

$$P_0=A_sF_y+A_c f'_{ce} \tag{4}$$

The table also gives the peak load obtained from the FE model analyses on the full-cross section, $P_{u,fem}$, the experimental load, $P_{u,exp}$, the test-to-predicted ratio for the ultimate load, the longitudinal strain in the web at peak load as obtained from the analysis, $\varepsilon_{u,fem}$, and from the experiments, $\varepsilon_{u,exp}$, and the test-to-predicted ratio for the longitudinal strain. The FE models give a very good estimate of the ultimate capacity of the columns when using a concrete strength equal to f'_{ce}, the test-to-predicted ratio ranging from 0.96 (C-10) to 1.06 (P-5) with a mean of 1.00. The load ratio for specimen P-5 is relatively high but this result can be attributed to the uncertainty in the concrete strength for that column and, therefore, was not included in the calculation of the statistical values.

Table 4 also shows that the FE models generally give higher strains at peak load, with an average experimental to numerical ratio of 0.95. The reason for this is that the FE strain represents the average strain over a column segment of height s in which failure takes place. In the test columns, the strains were obtained from LVDT measurements of the axial deformation of the specimens over nearly their total height. Failure in test columns typically occurred over 1/5 of the specimen height and hence, experimental strains near peak load include the strains due to inelastic unloading outside of the failed area. Moreover, in order to avoid end failure in the test columns, higher strength concrete was used at both ends of the column specimens, reducing further the experimental average strain.

5.2. Axial load-strain behaviour of composite models

Fig. 8 compares the experimental and numerical load-strain responses of representative specimens

Table 4 Results at peak load of plastic analyses of composite models with a concrete strength of f'_{ce}

Test Series	Spec.	P_0 (kN)	$P_{u,fem}$ (kN)	$P_{u,exp}$ (kN)	$P_{u,exp}/P_{u,fem}$ (-)	$\varepsilon_{u,fem}$ (με)	$\varepsilon_{u,exp}$ (με)	$\varepsilon_{u,exp}/\varepsilon_{u,fem}$ (-)
1	C-2	9 938	9 889	10 100	1.02	2 500	2 306	0.92
	C-4	9 813	9 450	9 390	0.99	2 235	1 695	0.76
	C-5	10 189	10 189	10 000	0.98	2 380	2 330	0.98
	C-7	4 447	4 225	4 280	1.01	2 141	2 142	1.00
2	C-8	17 623	16 742	16 470	0.98	2 050	1 845	0.90
	C-9	17 623	16 671	16 610	1.00	2 150	1 769	0.82
	C-10	17 557	16 995	16 240	0.96	2 285	2 256	0.99
	C-11	15 308	14 206	14 930	1.05	2 090	1 810	0.87
	C-12	18 009	17 540	17 450	0.99	2 310	2 580	1.12
3	P-1	4 948	4 725	4 770	1.01	2 353	2 335	0.99
	P-2	4 948	4 716	4 670	0.99	2 717	2 730	1.01
	P-3	4 948	4 712	4 790	1.02	2 878	2 550	0.93
	P-4	4 948	4 708	4 975	1.06	3 020	2 910	1.01
	P-5	9 131	8 680	9 225	1.06	2 750	2 820	1.03
Mean*					1.00			0.95
SD*					0.03			0.09

Note: *Column P-5 not included

obtained using a concrete strength of $\Psi f'_c$ and $0.92\Psi f'_c$. The results show the effects of the specimen size (C-7 vs. C-9), the link spacing and additional reinforcement (C-9 vs. C-12), the plate slenderness (C-9 vs. C-11), and long-term effects (P-1 vs. P-3). Overall, a very good agreement on the elastic column stiffness, the peak load and the strain at peak load was obtained between the experiments and FE models when an effective concrete strength $f'_{ce}=0.92\Psi f'_c$ was specified.

For test Series 3 specimens subjected to long-term loading (P-2 to P-5), the prediction at the end of loading Stage 2 is represented by the hollow symbols in the figure. As shown, it compares well with the corresponding experimental data point. For all specimens, the response could not be reproduced far beyond the peak load due to numerical convergence problems that occurred. However, a negative stiffness was obtained at the end of all analyses, indicating that the analysis had reached the post-peak domain.

5.3. Influence of residual stresses and initial imperfections on material efficiency

Table 5 gives the ultimate load normalised to P_0 and the computed average stresses at peak load in the flanges, σ_{fl}, the web, σ_w, and the concrete, σ_c. These stresses were obtained by dividing the total load acting on each component by its cross-section area. They were then normalised to F_y for the steel and to f'_{ce} for the concrete to obtain stress efficiency ratios. Table 6 presents the results of a study on the sensitivity of representative specimens (different d, s/d, and b/t) to residual stresses and local imperfections. Case 1 in the table corresponds to the actual test conditions with $\delta_0=\delta_{0m}$ and $\sigma_r=\sigma_{rm}$. In Cases 2 and 3, the effects of setting respectively the residual stresses and the initial imperfections to zero were examined. Cases 4 and 5 were considered to study the influence of increasing the amplitude of initial

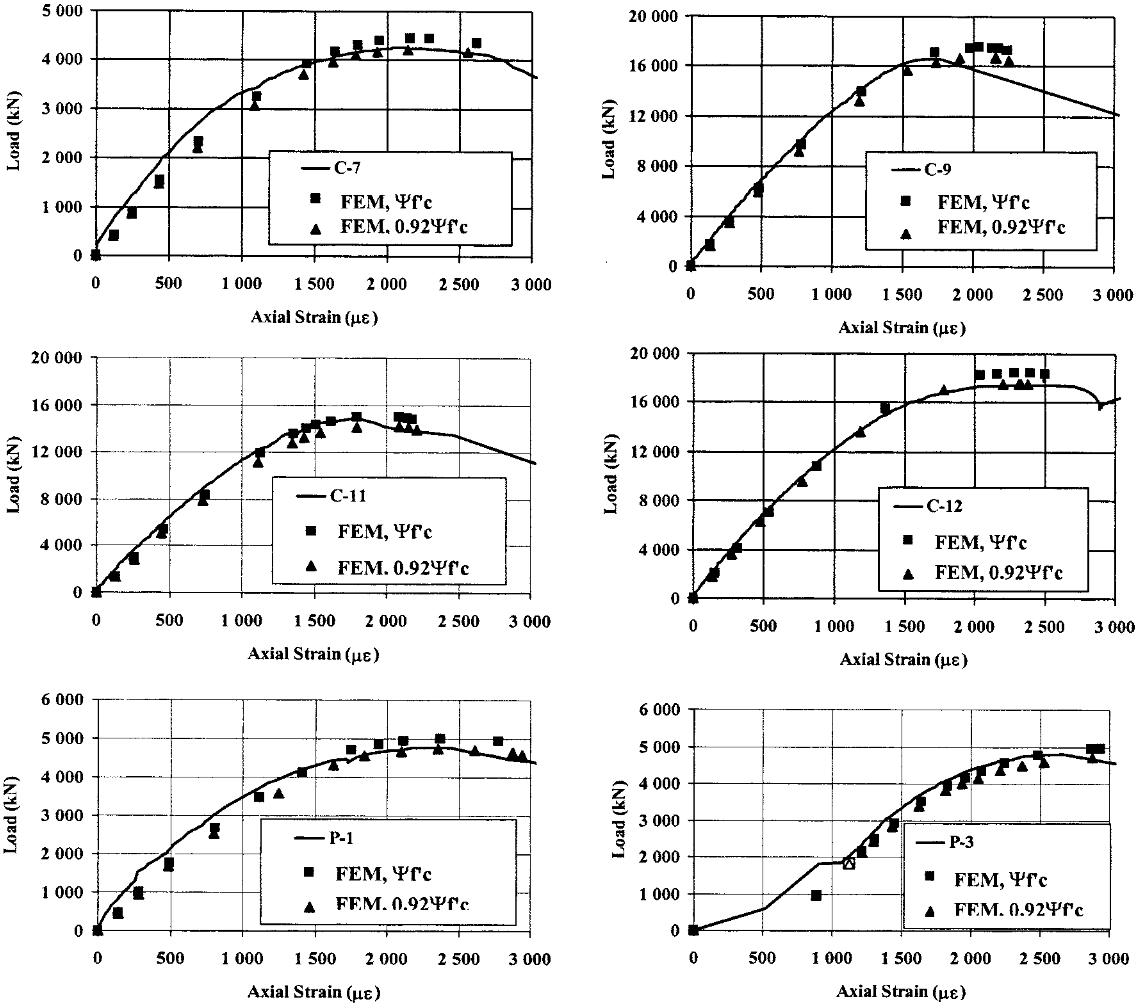

Fig. 8 Load-strain behaviour of specimens and FE models

imperfections (Case 4: $\delta_0 = 3\delta_{0m}$) and specifying inward imperfections (Case 5: $\delta_0 = -\delta_{0m}$).

5.3.1. Stress efficiency ratio for the flange under short-term loading

Table 5 shows that the stress efficiency ratio of the flange (σ_{fl}/F_y) varies from 0.75 to 0.97, with a mean value of 0.88. It is generally higher for specimens with $s=d/2$ than for specimens with $s=d$ (e.g., 0.97 for C-2 vs. 0.88 for C-4). It is also higher for specimens with a lower b/t ratio (0.86 for C-8 vs. 0.75 for C-11). These two observations are typical for local buckling behaviour as the flange slenderness increases with s/d and b/t.

Table 5 also shows that the stress ratio for the flanges does not vary much with the size of the columns when s/d and b/t are kept constant. For instance, σ_{fl}/F_y ranges from 0.85 to 0.88 for all specimens with $s=d$ and b/t=23, and it varies from 0.92 to 0.97 for specimens with $s=d/2$. These slight variations in the stress ratio with d are attributed to the aforementioned differences in the modelling of the residual

Table 5 Normalized load and stresses at peak load for flange, web, and concrete

No.	$P_{u,fem}/P_0$(-)	σ_{fl}/F_y(-)	σ_w/F_y(-)	σ_c/f'_{ce}(-)
C-2	1.00	0.97	0.96	1.02
C-4	0.96	0.88	0.95	1.02
C-5	1.00	0.97	0.96	1.03
C-7	0.95	0.87	0.87	1.02
C-8	0.95	0.86	0.94	1.01
C-9	0.95	0.85	0.95	1.00
C-10	0.97	0.92	0.94	1.01
C-11	0.93	0.75	0.94	1.00
C-12	0.97	0.92	0.94	1.01
P-1	0.96	0.88	0.88	1.02
P-2	0.95	0.87	0.91	1.01
P-3	0.95	0.87	0.93	1.00
P-4	0.95	0.85	0.94	1.01
P-5	0.95	0.86	0.97	1.00
Mean*	0.96	0.88	0.93	1.01
SD*	0.02	0.05	0.03	0.01

Note: *Analysis P-5 not included

tensile stresses from one column to another. The steel in the regions of the cross-section subjected to high tensile residual stresses does not reach the yield stress at peak load, when crushing of the concrete occurs. This contributes in reducing the efficiency of the steel shape and any variation in the modelling of the tensile residual stresses has an influence on the flange efficiency ratio. Therefore, the observed variations with d could have been induced by the limitations imposed by the model.

In the tests, the compressive residual stresses contributed in reducing the efficiency of the steel flanges by promoting inelastic local buckling of the flanges. It is believed that this effect was adequately captured by the model, considering the good match between the experimental and analytical compression residual stresses. Nevertheless, in order to eliminate the dependency of the model to tensile residual stresses, Cases 1 and 2 are compared in Table 6 for columns with the same residual stress pattern (Fig. 6: C-2 vs. C-4 and C-8 vs. C-10) to assess the influence of these stresses on the behaviour of the columns. It can be seen that neglecting residual stresses in these specimens leads to a similar increase of the stress ratio for a given pattern: 1% for C-2 vs. 3% for C-4, and 7% for both C-8 and C-10. The increase in stress ratio is larger, however, for the 600 mm columns because relatively higher tensile residual stresses were included in the models for these columns. Overall, the influence of both the compressive and tensile residual stresses resulted in a decrease of the flange capacity of 1% (C-2) to 8% (C-11), with an average of 5%.

Comparing cases 1 to 3 in Table 6 shows that the flange capacity was also reduced by the presence of local initial imperfections. This reduction is more important for specimens with $s=d$ than for specimens with $s=d/2$: 6% for C-42 vs. 2% for C-2, and 4% for C-8 vs. 1% for C-10. This can be explained by the fact that the measured flange imperfections were typically greater in specimens with $s=d$. In addition, the slenderness of the flanges in specimens with $s=d/2$ was lower, as indicated by a stress ratio closer to unity in Table 6. Hence, local imperfections had limited effects for these columns. For specimen C-11, with a b/t ratio of 31, the local imperfections had negligible effects because the flange buckled nearly

Table 6 Sensitivity of stress efficiency ratios to residual stresses and local imperfections

Specimen	Parameter d_0= σ_r=	Case 1 δ_{0m} σ_{rm}	Case 2 δ_{0m} 0	Case 3 0 σ_{rm}	Case 4 $3\delta_{0m}$ σ_{rm}	Case 5 $-\delta_{0m}$ σ_{rm}
C-2	$P_{u,fem}/P_0$	1.00	1.00	1.00	0.99	1.00
d=450	σ_{fl}/F_y	0.97	0.98	0.99	0.94	0.99
s=d/2	σ_w/F_y	0.96	0.96	0.96	0.96	0.97
b/t=23	σ_c/f'_{ce}	1.02	1.02	1.02	1.02	1.02
C-4	$P_{u,fem}/P_0$	0.96	0.97	0.98	0.94	1.00
d=450	σ_{fl}/F_y	0.88	0.91	0.94	0.82	0.99
s=d	σ_w/F_y	0.95	0.95	0.96	0.95	0.96
b/t=23	σ_c/f'_{ce}	1.02	1.02	1.02	1.02	1.02
C-8	$P_{u,fem}/P_0$	0.95	0.98	0.96	0.94	0.97
d=600	σ_{fl}/F_y	0.86	0.93	0.90	0.81	0.93
s=d	σ_w/F_y	0.94	0.96	0.93	0.94	0.95
b/t=23	σ_c/f'_{ce}	1.01	1.01	1.01	1.01	1.01
C-10	$P_{u,fem}/P_0$	0.97	1.00	0.97	0.97	0.97
d=600	σ_{fl}/F_y	0.92	0.99	0.93	0.91	0.93
s=d/2	σ_w/F_y	0.94	0.97	0.94	0.94	0.94
b/t=23	σ_c/f'_{ce}	1.01	1.02	1.01	1.01	1.01
C-11	$P_{u,fem}/P_0$	0.93	0.95	0.93	0.93	0.97
d=600	σ_{fl}/F_y	0.75	0.83	0.75	0.73	0.90
s=d	σ_w/F_y	0.94	0.96	0.94	0.94	0.95
b/t=31	σ_c/f'_{ce}	1.00	1.00	1.01	1.01	1.01
P-1	$P_{u,fem}/P_0$	0.96	0.97	0.97	0.94	0.99
d=300	σ_{fl}/F_y	0.88	0.91	0.94	0.83	0.97
s=d	σ_w/F_y	0.88	0.95	0.89	0.88	0.90
b/t=23	σ_c/f'_{ce}	1.02	1.02	1.02	1.02	1.02

elastically. Overall, for the 6 specimens described in Table 6, local imperfections decreased the capacity of the flanges by as much as 6% with an average reduction of 3%.

Increasing the initial flange imperfections up to three times those measured on the test columns (Case 4) reduced further the flange capacity. Again, the reduction is greater for specimens with $s=d$ than for specimens with $s=d/2$, as shown when comparing Cases 3 and 4 (5% for C-2 vs. 12% for C-4 and 9% for C-8 vs. 2% for C-10). The average imperfections for the four specimens with $s=d$ in Table 6 is s/500, which approximately corresponds to three times the limit of $s/200$ specified in CSA (2001). For these specimens, the flange capacity and the overall column strength decreased by up to 6% and 2%, respectively, when amplifying three times the imperfections. This result is considered later when establishing the design equation. Table 6 also shows the effects of specifying inward flange imperfections, as measured experimentally (Case 5). No significant change in flange capacity was obtained for specimens with $s=d/2$ but important benefits were observed for the $s=d$ specimens with σ_{fl}/F_y increasing from 9% to 15%. In view of the inability of the model to accurately reproduce the large concrete expansion near peak load, and its detrimental effects on flange stability, it is recommended that this increase be neglected until further studies with more realistic numerical models are performed.

5.3.2. Stress efficiency ratio for the web under short-term loading

In Table 5, the stress efficiency ratio for the web (σ_w/F_y) for all 450 mm and 600 mm specimens ranges from 0.94 to 0.96, indicating a negligible influence of the column size and link spacing on the web capacity. This was expected as the web is prevented from buckling in the column. The web stress ratio is lower for the 300 mm specimens C-7 and P-1 (0.87 and 0.88 for C-7 and P-1, respectively) but this can be attributed to the difficulty in modelling with precision the tensile residual stresses, as explained earlier.

The effects of residual stresses on the web capacity can be assessed by comparing Cases 1 and 2 in Table 6. Because web buckling is not possible, only the tensile residual stresses impact on the web efficiency and the results show that these stresses result in a reduction varying from 0 to 3% for the 450 and 600 mm columns and reaching 7% for the 300 mm P-1 column.

In Case 2, it can also be noted that the efficiency ratio without residual stresses is still lower than 1.0. The missing capacity ranges from 3% for specimen C-10 to 5% in column P-1 and is due to the detrimental effects of transverse tensile stresses that develop in the web, as discussed in section 5.4. Table 6 also shows that, as expected, flange local imperfections had no effect on the stress ratio of the web.

5.3.3. Stress efficiency ratio for the concrete core under short-term loading

In Table 5, the stress efficiency ratio for the concrete (σ_c/f'_{ce}) is close to one, indicating no significant gain in axial capacity due to concrete confinement (maximum stress ratio of 1.03 for specimen C-5). Localized confinement effects were observed only in the close vicinity of the welds and at the transverse links, near the flange. As shown in Fig. 9, the axial stresses at peak load in the models ranged locally from 0.9 f'_{ce}, in regions where transverse tensile stresses were present, to 1.3 f'_{ce} in zones of maximum confinement. These findings suggest that concrete confinement should be ignored in the design of this type of columns.

5.4. Influence of concrete transverse expansion under short-term loading

The transverse expansion of the concrete upon axial loading induces tensile axial stresses in the transverse links and transverse tensile stresses in the web of the steel shape.

5.4.1. Tensile axial stresses in the transverse links

Fig. 10 compares the variation of the experimental and numerical transverse link axial stresses up to peak load as a function of the average longitudinal strain of the column. The experimental results are from Chicoine *et al*. (2002a, 2002b). Tension stresses are shown as positive. Good agreement is generally obtained between the numerical and experimental results, indicating that the axial link stresses mainly depends on the transverse expansion of the concrete. Some variation were observed which can be attributed to localized effects, such as non uniformity of the bond along the length of the link during the test. In Specimen C-10, the experimental link stresses near peak load are higher than the predicted value. For this specimen, the failure zone occurred away from the instrumented links, and the built-in concrete model in ABAQUS underestimated the concrete expansion at large longitudinal strains.

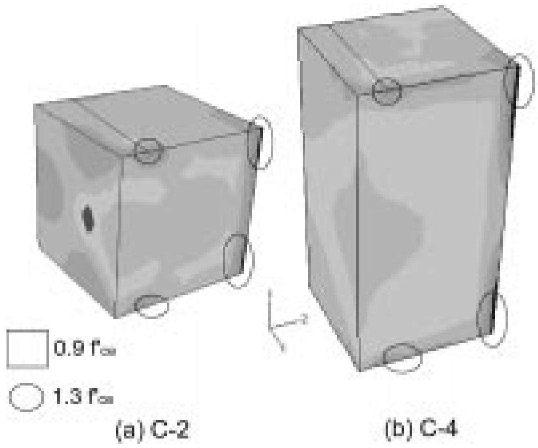

Fig. 9 Axial stresses in the concrete at peak load for specimens

5.4.2. Transverse stresses in the web

Fig. 11 compares the variation of the experimental and FE model transverse stresses in the web with the average longitudinal column strain. The stresses are examined at the intersection of the two axes of symmetry of the cross-section and at two different heights: at the links and halfway between two consecutive links. The model results are from the analyses with a concrete strength equal to f'_{ce} and

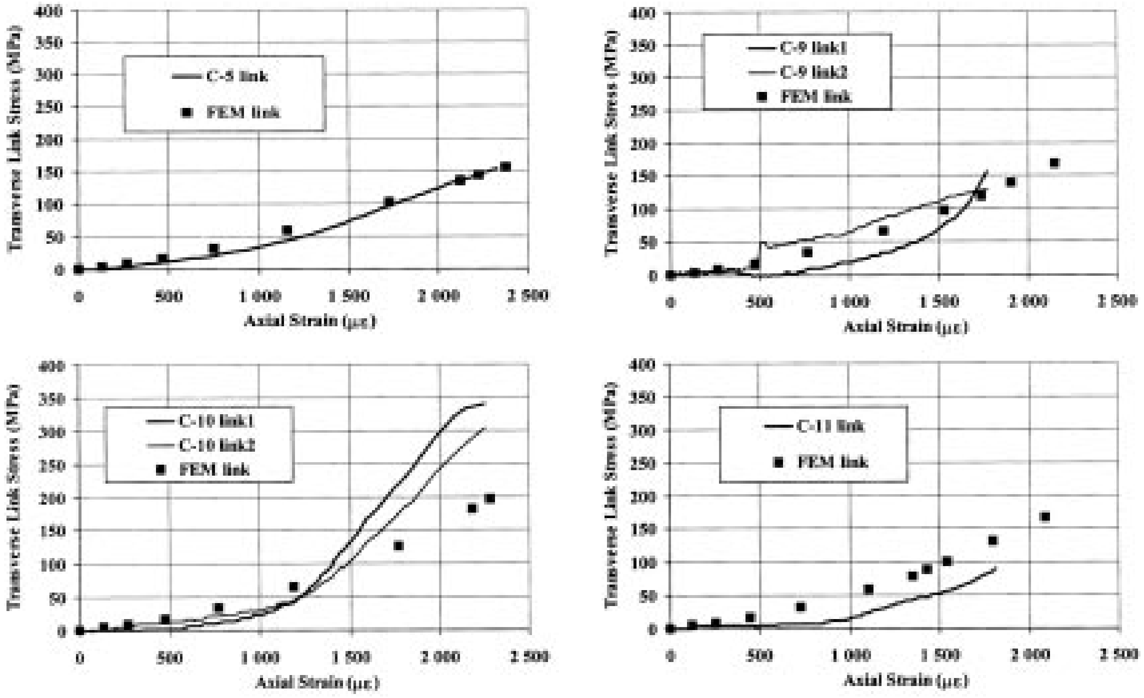

Fig. 10 Stresses in the transverse links of specimens and FE models

transverse stresses are positive in tension. The numerical and experimental transverse stresses in the web are plotted up to the peak load but the experimental transverse stresses were considered to remain constant after the von Mises yield criteria was met in the web.

A similar behaviour was observed in all FE models for the web transverse stresses, reflecting the effects of the variable concrete Poisson's ratio. Transverse expansion of concrete is smaller than that of steel until approximately 70% of the concrete strength is reached. After this point, the Poisson's ratio of concrete becomes larger than that of steel. Near peak load, concrete expansion induces tensile transverse stresses in the web of the steel shape, reducing the web longitudinal yield capacity. Because web buckling was prevented, the transverse stresses are believed to be the only cause explaining web efficiency ratios ranging from 0.95 to 0.97 for Case 2 in Table 6. The experimental transverse stresses in the web near peak load are higher in some specimens, likely because the actual Poissonís ratio of the concrete in the columns was greater than 0.45 near peak load, which could not be reproduced by the numerical model. Furthermore, it is possible that the contact between the strain gauges on the web and the concrete in the test specimens was damaged near peak load, resulting in less accurate experimental data.

5.5. Effects of construction sequence and long-term loading

Fig. 11 shows that the transverse stresses in the web at peak load were approximately equal to 20 MPa under both long-term loading (specimen P-4) and short-term loading (specimen C-8). In Table 5, however, the efficiency ratio of the web increases for long-term loading compared to short-term loading (0.94 for P-4 vs. 0.88 for P-1). The additional compression axial stresses at peak load in the steel shape due to the sequence of loading and creep of the concrete contributed in diminishing the detrimental effects of the tensile residual stresses on the efficiency ratio of the web. This beneficial effect had, however, a small impact on the overall column capacity, as the load ratio $P_{u,fem}/P_0$ was nearly the same (≅0.95) for all Series 3 specimens.

The conditions affecting long-term behaviour in an actual building can be more critical than those prevailing in the test programme. For instance, the duration of loading in the test was limited to 150 days for practical considerations. For Specimen P-3, this resulted in a stress of 215 MPa in the steel at the end of loading stage 2 (Table 3). Under more severe conditions (e.g., longer loading time, lower relative humidity), that stress may increase up to 240 MPa for that type of column, as predicted with available creep and shrinkage models. When specifying this higher value, the FE model gave an axial capacity reduction of only 1% of $P_{u,fem}$. A similar behaviour is expected for specimens with different *d*, *s/d*, and *b/t* values, which suggests that the sequence of loading and long-term effects have no significant influence on the capacity of PEC columns and can be neglected in design.

5.6. Discussion on predicting column behaviour with d greater than 600 mm

An important aspect of finite element modelling is the ability to expand the use of the model out of the range of the parameters covered in the reference experimental programs. For example, it is likely that composite columns in actual buildings be larger than the maximum size tested. It is believed that the models developed in this study will predict adequately the behaviour of larger columns because:

- size effects on the concrete strength can be modelled adequately by using the effective concrete strength f'_{ce};
- the measured local flange imperfections were comparable in the 300 mm, 450 mm, and 600 mm specimens, suggesting that similar imperfections will be found in larger columns;

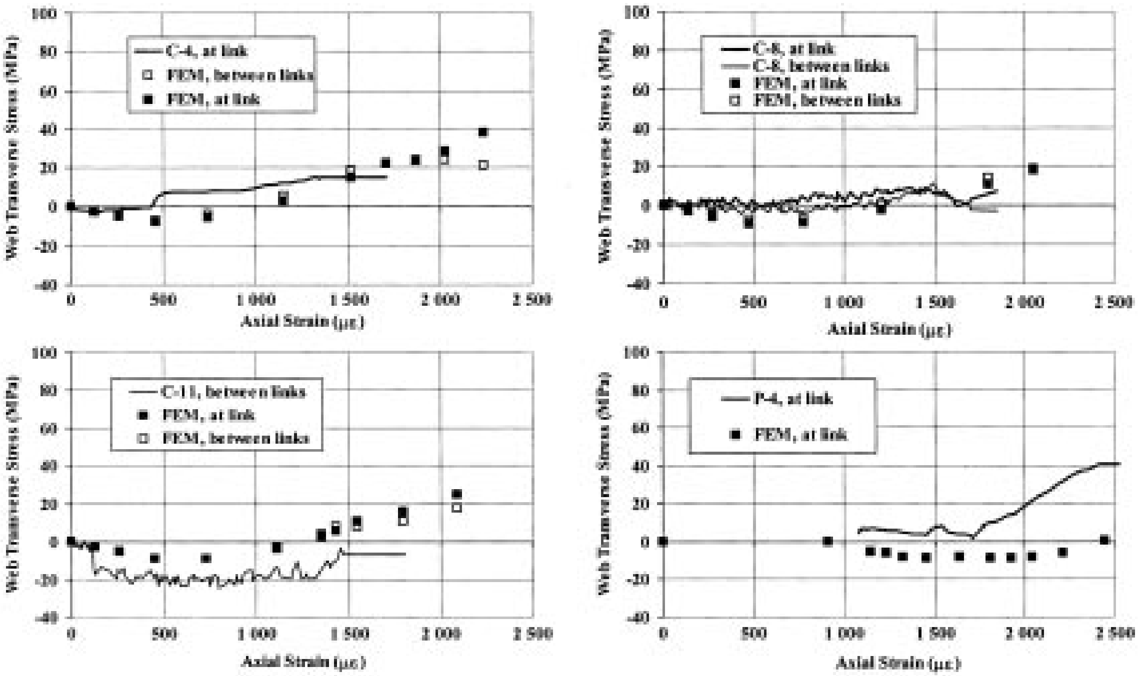

Fig. 11 Transverse stresses in the steel web of specimens and FE models

• the overall effects of the residual stresses on the column capacity are expected to generally decrease as the influence of the fabrication process (welding and cutting) on the residual stresses diminishes when the size of the column plates is increased.

6. Prediction model for the axial capacity

The axial capacity of composite columns can be obtained by summing up the contribution of each component, i.e., the steel shape, the concrete, and the reinforcing steel, if any. Tremblay *et al*. (2000) proposed such a formulation for PEC columns. This equation was based only on experimental data and is modified herein to reflect the additional information generated by the FE study. The revised expression is:

$$P_{u,pred} = A_{se}F_y + A_c f'_{ce} + A_r F_{yr} \tag{5}$$

$$A_{se} = (d-2t+4b_e)t \tag{6}$$

$$\frac{b_e}{b} = (1+\lambda_{fl}^{2n})^{(-1/n)}$$

$$\lambda_{fl} = \frac{b}{t}\sqrt{\frac{12(1-\nu^2)F_y}{\pi^2 E k_{fl}}} \tag{8}$$

$$k_{fl} = \frac{3.6}{(s/b)^2} + 0.05(s/b)^2 + 0.75, \qquad 1 \le s/b \le 2 \tag{9}$$

In Eq.(5) the contribution of the steel shape is based on the effective steel area for local buckling, A_{se}, and the contribution of the concrete is determined using the effective strength as defined in Eq. (1). In this equation, A_c and A_r are the cross section area of the concrete and the longitudinal rebars, respectively, and F_{yr} is the yield stress of the steel reinforcement. The parameter n may be taken as 1.5 for design, as discussed below. The effective concrete strength, f'_{ce}, accounting for concrete size and quality, is set to $0.92\Psi f'_c$, where Ψ is given in Eq. (3).

The effective area of steel, A_{se}, is given by Eq. (6). In this equation, the web is assumed to be fully effective although the FE analyses showed that the residual stresses and transverse stresses could reduce its capacity by 5% on average (Table 6). For simplification, this reduction in the web capacity has been assigned to the flanges by including it in the calculation of the effective width of the flange, b_e. This simplification is deemed acceptable because the flange has twice the area of the web, which results in a small variation on b_e. From the test results, values for b_e were computed with Eqs. (5) and (6), taking $P_{u,pred}$ equal to $P_{u,exp}$, and are presented in Fig. 12 as a function of the plate slenderness λ_{fl}, as given in Eq. (8). As shown, the experimental values of b_e are in close agreement with stress efficiency ratio of the flanges (b_e/b taken as σ_{fl}/F_y in Table 5) and with several empirical plate buckling models proposed in past research (Winter 1968, Faulkner 1977, Usami and Fukumoto 1982, Fukumoto *et al.* 1984, Ge and Usami 1992, and Uy 2000). Obtaining such reasonable values of b_e, while assuming a fully effective web, supported the use of this simplified approach in the design of PEC columns. The figure also shows that assuming a concrete strength of $\Psi f'_c$ gives unrealistic estimates of the buckling strength of the steel plates when compared to the other models. This again confirms the relevance of using an effective concrete strength f'_{ce} of $0.92\Psi f'_c$. In this figure, the model by Tremblay *et al.* (2000) is also presented and is shown to be too conservative.

Eq. (9) for the plate stiffness coefficient, k_{fl}, was derived empirically from elastic buckling analysis of FE models of steel column flanges, with fixed boundary conditions on three sides and free on one unloaded edge (Chicoine *et al.* 2001). These values for k_{fl} were close to the theoretical values (Salmon and Johnson 1996) and typically smaller than those proposed by Tremblay *et al.* (2000).

Eq. (7) is proposed for the calculation of b_e/b in design. This equation is adapted from the column design curve expression proposed by Loov (1996) and implemented in the CSA-S16.1 Standard for the design of steel structures in Canada (1994b). As shown in Table 7, using n equal to 2.0 in Eq. (7) gives an average test-to-predicted ratio of 1.00, with a standard deviation of 0.03, for the ultimate axial capacity of all columns. Fig. 13 shows that the prediction model with n=2.0 is in close agreement with the experimental and numerical values, throughout the range of plate slenderness, including the capacity

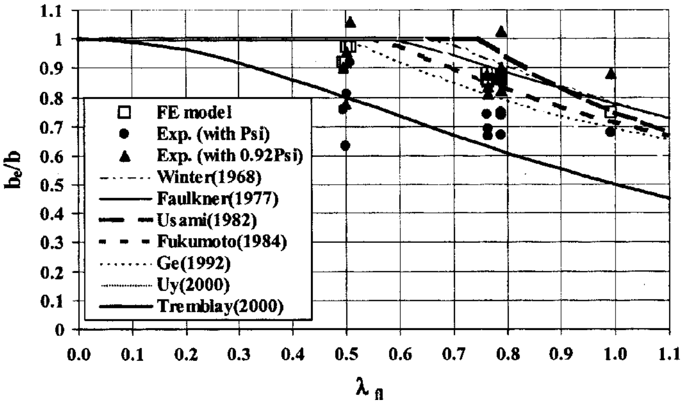

Fig. 12 Flange buckling capacity with plate slenderness

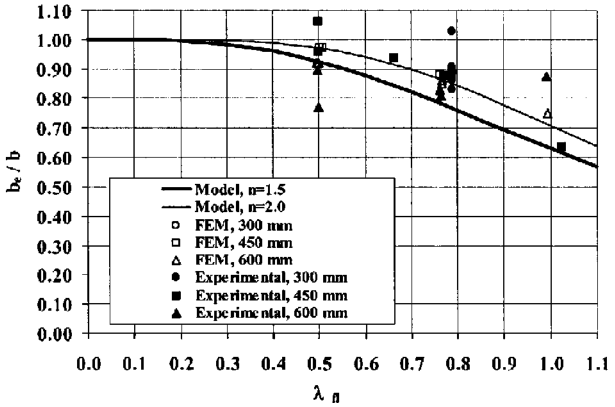

Fig. 13 Prediction model for flange effective width

Table 7 Test-to-predicted ultimate load ratios

Test Series	No.	k_{fl} (-)	λ_{fl} (-)	$P_{u,exp}$ (kN)	n=2.0		n=1.5	
					$P_{u,pred}$(kN)	$P_{u,exp}/P_{u,pred}$(-)	$P_{u,pred}$(kN)	$P_{u,exp}/P_{u,pred}$(-)
1 (Small Specimens)	C-2	4.40	0.50	10 111	9 815	1.03	9 664	1.05
	C-3	2.46	0.66	9 690	9 611	1.01	9 371	1.03
	C-4	1.85	0.77	9 389	9 321	1.01	9 050	1.04
	C-5	4.40	0.50	10 040	10 075	1.00	9 925	1.01
	C-6	2.46	1.02	7 652	7 757	0.99	7 593	1.01
	C-7	1.85	0.79	4 275	4 216	1.01	4 095	1.04
2 (Large Specimens)	C-8	1.85	0.76	16 470	16 770	0.98	16 308	1.01
	C-9	1.85	0.76	16 610	16 792	0.99	16 328	1.02
	C-10	4.40	0.50	16 240	17 337	0.94	17 082	0.95
	C-11	1.85	0.99	14 930	14 259	1.05	13 940	1.07
	C-12	4.40	0.50	17 430	17 846	0.98	17 591	0.99
3 (Long-Term Specimens)	P-1	1.85	0.79	4 770	4 697	1.02	4 568	1.04
	P-2	1.85	0.79	4 670	4 697	0.99	4 568	1.02
	P-3	1.85	0.79	4 790	4 697	1.02	4 568	1.05
	P-4	1.85	0.79	4 975	4 696	1.06	4 567	1.09
	P-5	1.85	0.75	9 225	8 711	1.06	8 465	1.09
Mean*						1.004		1.028
SD*						0.03		0.03

*Specimen P-5 not included

reduction for relatively stockier plates.

In order to account for the possibility that flange imperfections in actual columns be larger and approach the fabrication tolerances specified in CSA (2001) rather than being similar to those measured in the reference test columns, a value of n=1.5 is recommended for the calculation of b_e in design. As shown in Table 7, the mean test-to-predicted load ratio increased to 1.03, with a standard deviation of 0.03, when using n=1.5, which gives a sufficient margin to account for more critical imperfection conditions.

7. Conclusions

The conclusions regarding the parameters that were reproduced by the FE models are presented herein:

7.1. Capacity of the specimens under short-term loading

The mean numerical to experimental peak load ratio for Series 1, 2, and 3 composite specimens is equal to 1.00 when specifying an effective concrete strength f'_{ce}=0.92$\Psi f'_c$ in the numerical model. Such a resistance also permits to closely reproduce the experimental local buckling capacity of the flanges. At peak load, the average stresses carried by the flanges, the web, and the concrete were 0.88 F_y, 0.93 F_y, and 1.01 f'_{ce}, respectively. Buckling, together with compression residual stresses, initial imperfections, and high tensile residual stresses near the welds contributed in reducing the capacity of the flanges. The decrease in capacity due to residual stresses varied between 1 and 8% and the average reduction due to local imperfection was found to be 3%. In the web, the reduction in capacity is attributed to the combined effects of the tensile residual stresses that exist near the welds (up to 3% for the large columns) and of the tensile transverse stresses that develop due to the rapid expansion of the concrete near peak load (3-5%). The increase in concrete strength due to localised confinement effects is small (1.01 f'_{ce}) and can be neglected in design.

7.2. Strain at peak load

The FE models represented very well the load-strain behavior of the test specimens throughout the loading history. The FE models gave values of the strain at peak load 5% higher, on average, than those measured in the experiments. This apparent discrepancy is due to the fact that the experimental strains were measured over the full height of the column, including the zones with higher strength concrete, while the model strains were taken over the height of one link spacing only. The post-peak response of the columns could be obtained only over a short deformation range due to convergence problems in the numerical model.

7.3. Failure modes

The failure modes in the FE analyses were identical to the experimental ones and good agreement for the ultimate load was obtained when local flange imperfections were modelled outwards instead of inwards, as measured on the reference test columns. Different buckling modes and higher capacity were obtained when setting the imperfections inwards. This is attributed to the incapacity of the FE model adopted to reproduce the rapid volumetric expansion of concrete near peak load.

7.4. Axial stresses in the transverse links

The stresses in the transverse links were well represented by the numerical models and were found to be dependent on the transverse expansion of the concrete. At peak load, however, the numerical models generally underestimated the experimental link stresses because of the limitations imposed on the expansion of the concrete.

7.5. Transverse stresses in the web of the steel shape

As found in the experimental program, the FE model produced transverse stresses in the web that were compressive at the beginning of the analysis and then tensile at peak load, due to the variation of the concrete Poissonís ratio.

7.6. Loading sequence and long-term effects

The FE program was capable of modelling satisfactorily the construction sequence, by removing and adding elements in the model. The effects of creep and shrinkage of the concrete on the steel shape were modelled by increasing the stresses in the model that included the steel shape only, prior to composite action. These effects were found not to influence the axial capacity of the columns, as also observed in the tests.

Based on the findings of this study, a new expression was proposed to predict the axial capacity of PEC columns for design purposes. It is recommended that further study be pursued to better capture the effects of the rapid expansion of the concrete near peak load on the flange buckling capacity and on the amplitude of transverse stresses in the web.

Acknowledgements

Funding for this research was provided by the Natural Science and Engineering Research Council of Canada (NSERC), the Steel Structures Education Foundation, and the Canam Manac Group.

References

Bloem, D. (1968), “Concrete strength in structures”, *ACI Journal*, 65-14, 176-187.

Bouzaiene, A. and Massicotte, B. (1997), “Programme MEF97 Manuel díutilisation”, *EPM/CS No. 1997-2*, Dept. of Civil, Geological and Mining Engineering, Ecole Polytechnique, Montreal, Canada. Draft version.

Broderick, B.M. and Elnashai, A.S. (1994), “Seismic resistance of composite beam-columns in multi-storey structures. Part 2: analytical model and discussion of results”, *J. Construct. Steel Research*, **30**, 231-258.

Chicoine, T., Tremblay, R., Massicotte, B., Yalcin, M., Ricles, J. and Lu, L.-W. (2000a), “Test programme on large-scale partially-encased built-up three-plate composite columns”, *Joint Report, EPM/GCS No. 2000-06*, Dept. of Civil, Geological and Mining Engineering, Ecole Polytechnique, Montreal, Canada ñ ATLSS Engineering Research Center, *No. 00-04*, Lehigh University, Bethlehem, Pennsylvania, USA.

Chicoine, T., Tremblay, R., Massicotte, B. (2000b), “Long-term test programme on partially encased built-up three-plate composite columns”, *EPM/GCS No. 2000-20*, Dept. of Civil, Geological and Mining Engineering, Ecole Polytechnique, Montreal, Canada.

Chicoine, T., Massicotte, B. and Tremblay, R. (2001), “Finite element modelling of the experimental response of partially encased composite columns”, *EPM/GCS No. 2001-06*, Dept. of Civil, Geological and Mining Engineering, Ecole Polytechnique, Montreal, Canada.

Chicoine, T., Tremblay, R., Massicotte, B., Ricles, J.M. and Lu, L.-W. (2002a), “Behavior and strength of partially encased columns with built-up shape”, *J. Struct. Eng.*, ASCE, **128**(3), 279-288.

Chicoine, T., Massicotte, B. and Tremblay, R. (2002b), “Long-term behaviour and strength of partially encased composite columns made with built-up steel shapes”, *J. Struct. Eng.*, ASCE. In press.

CSA (1994a), *CAN/CSA-A23.3-94 Code for the Design of Concrete Structures for Buildings*. Canadian Standards Association, Rexdale, Ontario.

CSA (1994b), *CAN/CSA-S16.1-94 Limit States Design of Steel Structures*. Canadian Standards Association, Rexdale, Ontario.

CSA (2001), *CAN/CSA-S16.1-01 Limit States Design of Steel Structures*. Canadian Standards Association, Rexdale, Ontario. (Publication pending)

Faulkner, D. (1977), "Compression tests on welded eccentrically stiffened plate panels", *Steel Plated Structures*, P.J. Dowling Ed., London, 581-617.

Fukumoto, Y., Itoh, Y. (1984), "Basic compressive strength of steel plates from test data", *Proc. JSCE*, No 344, April, 129-139.

Ge, H., Usami, T. (1992), "Strength of concrete filled thin walled steel box columns: Experiment", *J. Struct. Eng.*, ASCE, **118**(11), 3036-3054.

HKS (2000), *Abaqus program version 5.8-19.*

Loov, R. (1996), "A simple equation for axially loaded steel column design curve", *Can. J. Civ. Eng.*, **23**, 272-276.

Maranda, R. (1999), "Analyses par éléments finis de poteaux mixtes avec sections díacier en I de classe 4", *Report n^o. EPM/GCS-1998-11*, Dept. of Civil, Geological and Mining Engineering, Ecole Polytechnique, Montreal, Canada, 139 p.

Neville, A.M. (1966), "A general relation for the strengths of concrete specimens of different shapes and sizes", *ACI Journal* **63**, 1095-1108.

Newman, K. (1987), "Labcrete, Realcrete, and Hypocrete. Where we can expect the next durability problems", *ACI SP-100 Concrete Durability*, **2**.

Salmon, C.G., Johnson, J.E. (1996), *Steel Structures: Design and Behavior*, HarperCollins, 4th Edition, New York, NY.

Sigiura, K., Ono, K., Oyawa, W.O., Watanabe, E. and Yamaguchi, T. (2000), "Interface interaction in filled steel tubular members as modeled by open sandwich beams", *Proc. Composite Construction IV*, Engineering Foundation, Banff, Canada.

Tremblay, R., Massicotte, B., Filion, I. and Maranda, R. (1998), "Experimental study on the behavior of partially encased composite columns made with light welded H steel shapes under compressive axial loads", *1998 SSRC Annual Technical Meeting.*

Tremblay, R., Chicoine, T. and Massicotte, B. (2000), "Design equation for the axial capacity of partially encased non-compact columns", *Proc. Composite Construction IV*, Engineering Foundation, Banff, Canada.

Tsai, W.T. (1988), "Uniaxial compression stress-strain relation of concrete", *J. Struct. Eng.*, ASCE, **114**(9), 2133-2136.

Usami, T. and Fukumoto, Y. (1982), "Local and overall buckling of welded box columns", *J. Struct. Div.*, ASCE, **108**(3), 525-542.

Uy, B. (2000), "Strength of concrete filled steel box columns incorporating local buckling", *J. Struct. Eng.*, ASCE, **126**(3), 341-352.

Vincent, R. (2000), "Design and application of partially encased non-compact composite columns for high-rise buildings", *Proc. Composite Construction IV*, Engineering Foundation, Banff, Canada.

Wheeler, A.T. and Bridge, R.Q. (2000), "Thin walled steel tubes filled with high strength concrete in bending", *Proc. Composite Construction IV*, Engineering Foundation, Banff, Canada.

Winter, G. (1968), "Thin-walled structures ñ theoretical solutions and test results", *Proc. IABSE Congress*, 101-112.

CU